Title: Electron localization of gold in control of nitrogen-to-ammonia fixation

Authors: Yafei Li; Jianyun Zheng; Yanhong Lyu; Man Qiao; Jean P Veder; Roland D Marco; John Bradley; Ruilun Wang; Aibin Huang; San Ping Jiang; Shuangyin Wang

To be cited as: 10.1002/anie.201909477

Link to VoR: https://doi.org/10.1002/anie.201909477

Electron localization of gold in control of nitrogen-to-ammonia fixation

Jianyun Zheng,[†a,b,c] Yanhong Lyu,[†a,c] Man Qiao,[†d] Jean P. Veder,[e] Roland D. Marco,[b,f,g] John Bradley,[f] Ruilun Wang,[a,c] Yafei Li,*[d] Aibin Huang,*[h,i] San Ping Jiang,*[b] Shuangyin Wang*[a,c]

Abstract: The (photo)electrochemical N_2 reduction reaction (NRR) has gathered increasing attention because it provides a favorable avenue for the production of NH_3 using renewable energy in mild operating conditions. Understanding and building an efficient catalytic system with high NH_3 selectivity represents an area of intense interest for the early stages of development for NRR. Here, we introduce a CoO_x layer to tune the local electronic structure of Au nanoparticles with positive valence sites for boosting conversion of N_2 to NH_3. The catalysts, possessing high average oxidation states (~40%), achieve a high NH_3 yield rate of ~15.1 $\mu g \cdot cm^{-2} \cdot h^{-1}$ and a good faradic efficiency of 19% at -0.5 V versus reversible hydrogen electrode. Experimental results and theory simulations reveal that the ability to tune the oxidation state of Au enables control of N_2 adsorption and the concomitant energy barrier of NRR. The beneficial action of altering the Au oxidation state provides a unique strategy for control of NRR in the production of valuable NH_3 for energy and environmental applications.

Introduction

Nitrogen (N_2)-to-ammonia (NH_3) conversion using (photo)electrochemical methods represents an attractive alternative to the Haber-Bosch process for industrial-scale N_2 reduction under mild conditions. It also provides a means of storing renewable energy as NH_3, where NH_3 possesses a H_2 loading of with 17.6 wt%, representing a high volume energy density (13.6 $GJ \cdot m^{-3}$) with easy transportation characteristics[1]. Gold (Au) is arguably one of the most promising catalysts for the (photo)electrochemical N_2 reduction reaction (NRR)[2]. In recent years, researchers have experimented with the modification of Au metal (Au^0) by tuning the microstructure (like hollow nanocage)[3], crystalline structure (like amorphous Au)[4] and crystal facet (like (730) plane)[2a] has been deployed to yield variable quantities of NH_3 from N_2 at room temperature and atmospheric pressure. However, its poor activity and low selectivity are far from ideal with respect to the performance of NRR. Nevertheless, there remains considerable interest in further optimizing and modifying Au-based catalysts to increase the yield rate of NH_3 from NRR, ultimately scaling to industrial-sized production, and achieving such high yield rates in combination with high conversion of electricity-to-chemical fuels as a frontier technology in the field[5].

Surface oxidation state ($M^{\delta+}$) active sites in metallic catalysts have been proposed as playing a key role in (photo)electrochemical reduction reactions, and can bring in a redistribution of surface electron structure for enhancing the absorption ability of reactants and radical species[6]. Among these reactions, the most well-known one involves introduction of $Cu^{\delta+}$ into copper catalysts, so as to achieve a high efficiency of CO_2 conversion to C_2 hydrocarbons from electrochemical CO_2 reduction[7]. However, the implications of $M^{\delta+}$ on metal catalysts on the NRR is a scarcely studied subject, and there are no definitive clues about how $M^{\delta+}$ active sites might influence the mechanism of NRR[8]. Indeed, our preliminary work using theoretical calculations demonstrated that $Au^{\delta+}$ active sites may reduce the energy barriers of NRR, but this positive effect remains elusive experimentally due to the presence of aerophilic-hydrophilic hetero-structures[9].

Here we hypothesize that injection of a high oxidation state of Au (Au^{1+}) into Au nanoparticles (NPs) may contribute to enhancement of the efficacy for NRR and its practical functionality. The average oxidation state may be tuned using a thin layer of CoO_x as a dominant factor in boosting the efficiency and selectivity of N_2 reduction to NH_3. Doing so enabled us to achieve a high ammonia yield rate of ~15.1 $\mu g \cdot cm^{-2} \cdot h^{-1}$ and a good faradic efficiency (FE) of 19% at -0.5 V versus reversible hydrogen electrode (*vs* RHE). Meanwhile, a detailed catalytic mechanism of Au^{1+} on the electrochemical NRR has been elucidated by quasi in-situ x-ray photoelectron spectroscopy (XPS) and density functional theory (DFT).

Results and Discussion

A schematic illustration of the synthesis of the Au-based samples is presented in Figure 1a. A p-type boron-doped silicon

[a] Dr. J. Zheng, Dr. Y. Lyu, R. Wang, Prof. S. Wang
State Key Laboratory of Chem/Bio-Sensing and Chemometrics, College of Chemistry and Chemical Engineering, Hunan University, Changsha 410082, Hunan, China
E-mail: shuangyinwang@hnu.edu.cn
[b] Dr. J. Zheng, Prof. R. D. Marco, Prof. S. P. Jiang
Western Australian School of Mines: Minerals, Energy and Chemical Engineering and Fuels and Energy Technology Institute, Curtin University, Perth, WA 6102, Australia
E-mail: s.jiang@curtin.edu.au
[c] Dr. J. Zheng, Dr. Y. Lyu, R. Wang, Prof. S. Wang
The National Supercomputing Center in Changsha, Hunan University, Changsha 410006, China
[d] Dr. M. Qiao, Prof. Y. Li
Jiangsu Collaborative Innovation Centre of Biomedical Functional Materials, School of Chemistry and Materials Science, Nanjing Normal University, Nanjing 210023, China
E-mail: liyafei@njnu.edu.cn
[e] Dr. J. P. Veder
John de Laeter Centre, Curtin University, Perth, WA 6102, Australia
[f] Prof. R. D. Marco, Dr. J. Bradley
School of Science and Engineering, University of Sunshine Coast, 90 Sippy Downs Drive, Sippy Downs, Queensland 4556, Australia
[g] Prof. R. D. Marco
School of Chemistry and Molecular Biosciences, The University of Queensland, Brisbane, Queensland 4072, Australia
[h] Dr. A. Huang
State Key Laboratory of High Performance Ceramics and Superfine Microstructure, Shanghai Institute of Ceramics, Chinese Academy of Sciences, Shanghai 200050, China
E-mail: huangab1990@163.com
[i] Dr. A. Huang
University of Chinese Academy of Sciences, Beijing, 100049, China

Supporting information for this article is given via a link at the end of the document.

(Si) wafer with (100) orientation was utilized as the substrate material, as described in the previous work of the authors[9-10]. Small-sized Au and Co islands were homogenously deposited onto the surface of Si using vapour deposition technology, and the Au NPs/CoO_x layer (labeled as Au/CoO_x) sample was formed by using fast annealing of 800 °C in air (Figure 1a). The cobalt oxide layer was selected as a means of introducing Au^{1+} active sites due to a strong charge exchange between cobalt oxide and gold[11]. In addition, we investigated the pure Au NPs on the Si wafer (labeled as Au sample) as a control experiment (Figure 1a). A range of samples at different Co loadings were also prepared, as shown in Supporting Information (SI). A detailed description of the synthetic method is provided in the Experimental Procedures of SI.

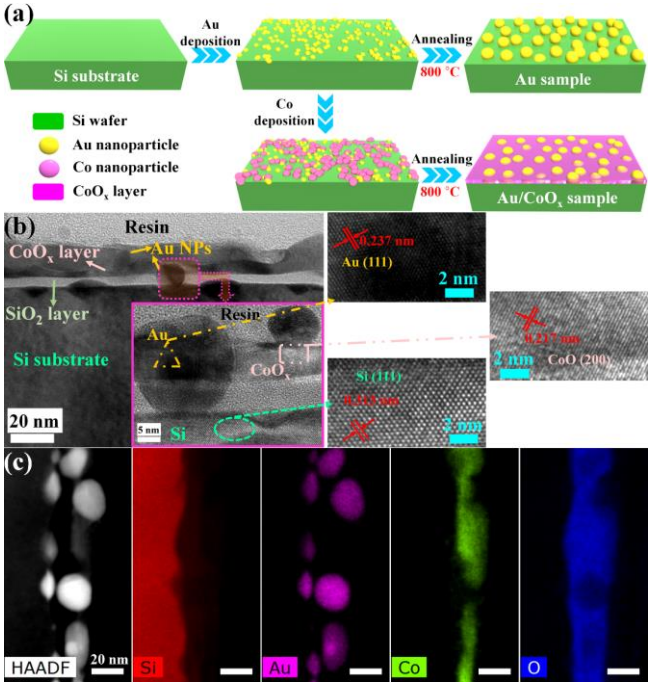

Figure 1. Synthesis and structural characterization of Au-based samples. (a) Schematic of the vapour deposition and annealing to fabricate the Au-based samples. (b) Cross-sectional TEM and HRTEM images of Au/CoO_x sample. The inset in TEM image is the magnified image of the specified area by HRTEM. High-magnification images on the right match in the marked area in the inset. (c) STEM image with corresponding elemental distribution maps for Au/CoO_x sample, with Si, Au, Co, and O labeled as red, pink, green, and blue, respectively.

The successful loading of crystalline Au onto all of the samples was confirmed by using grazing incidence x-ray diffraction (GIXRD, see Figure S1). Three peaks at around 38.2°, 44.4° and 64.6° are indexed to (111), (200) and (220) planes of Au (PDF no. 04-0784, JCPDS), respectively. By comparison to Au sample, Au/CoO_x sample showed more, broader and less intense peaks, implying that the Au NPs had more crystalline facets with smaller grain size (Figure S1). In addition, field emission scanning electron microscopy (FESEM) with energy dispersive spectroscopy (EDS) set at line-scanning mode was employed to outline the architecture of the samples (Figures S2-S5). Instead of coating the big Au NPs on the surface of Au sample (Figure S3a), Au NPs with a size less than 50 nm were dispersed on the surface of Au/CoO_x sample (Figure S2a). Additionally, a thin CoO_x layer surrounded the Au NPs with an approximate thickness of ~12 nm in the Au/CoO_x sample (Figure S2b). A similar architecture was also observed in other samples with different Co loadings (Figures S4-S5). High-resolution transmission electron microscopy (HRTEM) images (Figure 1b) indicated that the Au/CoO_x sample was composed of the Si substrate, a thin layer and NPs, in agreement with FESEM analysis. The lattice spacing of Si substrate, thin layer and NP was 0.313, 0.217 and 0.237 nm, respectively, corresponding to (111) plane of Si, (200) plane of CoO, and (111) plane of Au. The cross-section of Au/CoO_x sample (Figure 1c) was further detected using scanning transmission electron microscopy (STEM) coupled with EDS mapping. Elemental mapping showed that the thin CoO_x layer surrounded the bottom of the Au NPs, with the top portion of the Au NPs being directly exposed to the external environment.

Angle resolved and synchrotron radiation XPS (AR-XPS and SR-XPS, respectively) with tunable take-off angle (θ_{TO}) and photon energy (E_{Ph}) are powerful techniques to probe the atomic composition and electronic states of near-surface elements (from sub-nanometer to 10 nm depths) via non-destructive depth profiling[12]. With photoemission in XPS, the inelastic mean free path (IMFP) and concomitant distance travelled by photoelectrons before suffering inelastic scattering in the materials is fixed; however, at variable θ_{TO} in AR-XPS, the escape depth of photoelectrons (related to those electrons that are not inelastically scattered) is reduced at lower θ_{TO} values due to forcing the photoelectrons to skim from a shallower depth into the surface. Similarly, with E_{Ph} SR-XPS, the IMFP and concomitant escape depth of photoelectrons at fixed θ_{TO} is increased at higher photoelectron kinetic energies (and associated E_{Ph}), thereby leading to a skimming of photoelectrons at low E_{Ph} and a probing of deeper originating photoelectrons at higher E_{Ph}.

The full survey of the surface for Au/CoO_x sample from SR-XPS presents the characteristic peaks of Au 4f, Co 3p, Si 2p, C 1s and O 1s (see Figure S6). The atomic ratio of Co to Au for Au/CoO_x sample is ~8.2, as shown in Figure S7. For AR-XPS, by rotating the sample stage one can vary the θ_{TO} of photoelectron relative to the surface normal and in turn perform depth-dependent measurements. The Au 4f spectrum (Figure 2a) of Au/CoO_x sample at θ_{TO} of 90° were fitted into four peaks, where the peaks of Au 4f 7/2 at ~83.9 and ~85.1 eV represents metallic Au (Au^0) and positive Au species (Au^{1+}), respectively[9, 13]. The average oxidation state of Au, defined as the ratio of Au^{1+} to Au^0, was about 0.24. When the θ_{TO} was set at 10°, no Au^{1+} signal was identified. Meanwhile, Co 2p peaks of Au/CoO_x sample were hardly observed with decreasing the θ_{TO} from 90°

to 10° (Figure S8).By correlating the AR-XPS results and HRTEM images, we can imagine that the detectable area of the sample surface at θ_{TO} of 10° is concentrated on the topmost surface of Au NPs owing to self-shadowing effect (as described in the illustrations of Figure 2a). To further obtain the surface distribution of Au oxidation state and avoid the effect of the surface morphology, we also undertook depth profiling via SR-XPS to drive information on the spectra emitted from different E_{Ph} using SR-XPS[14]. The detectable depth of x-ray increases with its electron kinetic energy (related to photon energy) in the energy range higher than around 50 eV (in the illustrations of Figure 2c). Deconvolution of the Au 4f spectra of Au/CoO_x sample (Figure 2b) from SR-XPS with E_{Ph} of 150, 400 and 700 eV yielded two doublets, assigned to Au^0 and Au^{1+}. However, as shown in Figure 2c, the average oxidation state of Au was ~1.10, ~0.61 and ~0.45 corresponding to E_{Ph} of 150, 400 and 700 eV, respectively, signifying more Au^{1+} on the surface or subsurface (< 1 nm). The altered trend of average oxidation state with the increase of E_{Ph} was also discovered on other Au-based samples (Figures S9-S11). Surprisingly, there is a small amount of Au^{1+} (less than 0.1) on the surface or subsurface of Au sample, while the disappearance of Au^{1+} occurred in the bulk of Au sample (Figure 2a and Figure S9). This phenomenon for Au sample can result from the adsorption of oxidation species (like O_2 or OH^-) from ambient on the surface of Au NPs due to their high surface Gibbs free energy[15]. Regarding the Co 3p spectra for Au/CoO_x sample, two peaks at ~60.7 and ~63.4 eV (Figure S12) are evident and attributed to the existence of Co^{2+} and Co^{3+}, respectively. The Au/CoO_x sample measured at different E_{Ph} displayed the different ratios of Co^{2+} to Co^{3+}, which was proportional to the average oxidation state of Au. One can infer that the creation of Au^{1+} on the Au/CoO_x sample is attributed to the electron transfer from Au^0 into Co^{3+} in the fast annealing process in air. In addition, the number of sites with lower oxygen coordination (Peak β in Figure S13) were tuned with the change of electron structure of Co. As a result, on basis of the AR- and SR-XPS data, the Au^{1+} of Au/CoO_x sample mainly concentrate in the part of Au NPs encapsulated by the CoO_x layer and its distribution is more on the surface than in the bulk.

Valence band (VB) analysis of Au-based samples (Figure 2d and Figure S14) were also performed by SR-XPS to better clarify the electronic effect of Au^{1+} on catalytic activity. Tellingly, the near-Fermi level density of states (DOS) was sensitive to the local structural environment of Au in Figure 2d and Figure S14. Au sample showed a low DOS intensity in the near-Fermi level region with the edge of VB maximum at ~0.53 eV, being identical to the typical VB characteristics of Au. By contrast, a pronounced shift of VB maximum energy toward a deeper level is found on other samples with Au^{1+} (Figure S14). For Au/CoO_x sample with highest average oxidation state on the surface, the near-Fermi level DOS almost disappeared and the VB maximum energy was observed to be ~1.42 eV. The VB structure of Au-based samples can be closely related to their catalytic behaviour. Due to a shift of electron density from *d* orbitals to valence *s* orbital, Au^0 is less able to accept *σ*-donated electrons and engage in *π* back-donation for adsorbing the triple-bond molecules, like N_2 and carbon monoxide[16]. Nevertheless, the redistribution of DOS for Au^{1+} can be expected to strengthen the molecules on its surface. In order to further investigate the impact of Au oxidation state on the electronic transport characterization, we employed conductive atomic force microscopy (C-AFM) and temperature-dependent tunneling measurements. Apparently, high average oxidation states in the Au NPs, as in Au/CoO_x samples (Figure S15), give rise to a worse charge transfer than Au^0 or a low Au^{1+} concentration (Figures S16-S18), in good agreement with the VB structure. Meanwhile, apart from Au sample, the current density (*J*) of other Au-based samples (Figure S19) demonstrated a very little dependence on temperature (that is, -50 to 100 °C), strong indicative of the tunneling effect of electron transport[17].

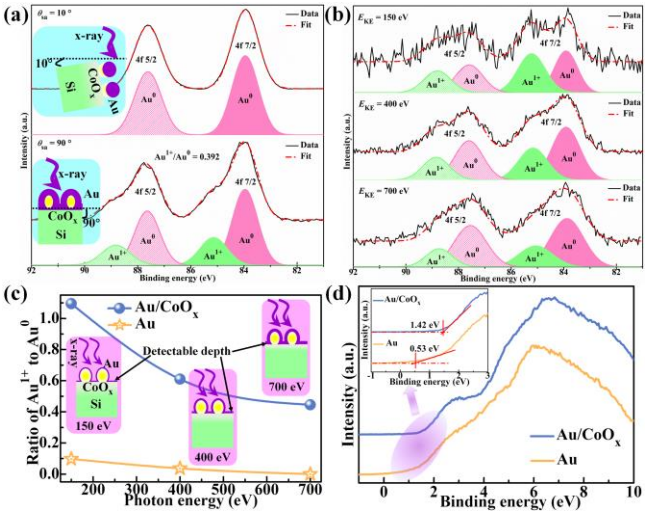

Figure 2. AR- and SR-XPS depth profile of Au-based samples. (a) Au 4f spectra of Au/CoO_x sample using AR-XPS with E_{Ph} of 1486 eV at θ_{TO} of 90° and 10°. The illustrations show the excitation situation of the sample at different θ_{TO}. (b) Au 4f spectra of Au/CoO_x sample using SR-XPS with E_{Ph} of 150 eV, 400 eV and 700 eV at θ_{TO} of 55°. (c) Ratio of Au^{1+} to Au^0 as a function of photon energy for the Au sample and Au/CoO_x sample. The illustrations outline the detectable depth of x-ray on the dependence of photon energy. (d) SR-XPS VB spectra of Au sample and Au/CoO_x sample with E_{Ph} of 70 eV and θ_{TO} of 55°. The inset is the high magnification image corresponding to the marked area by purple ellipse.

Electrochemical NRR measurements of Au-based samples were conducted in 0.05 M H_2SO_4 electrolyte through a H-type reaction cell including anodic compartment, cathodic compartment and proton conductive cation exchange membrane (Figure S20). To avoid N-sourced contamination from the environment, the exiting N_2 stream was bubbled through a water-filled vessel acting as a liquid seal[9]. The NH_3 yield was detected by an ammonia-ammonium ion selective electrode (ISE) (seen in the Experimental Section). Standard ammonium sulfate ($(NH_4)_2SO_4$) solutions with various known concentrations were used to establish a calibration curve for the NH_3 ISE, as

shown in Figure S21. The NH_3 yield rate and corresponding FE of Au and Au/CoO_x samples at given electrode potentials in a 10 h period are presented in Figure 3a. A NH_3 yield rate and FE of Au sample were in the range of 2.0-6.1 $\mu g \cdot cm^{-2} \cdot h^{-1}$ and 0.4%-5.4% at various applied potentials, respectively; however, after the introduction of Au^{1+}, both the NH_3 yield rate and FE of Au/CoO_x sample increased dramatically by almost 2.5 and 3.5 times, respectively. The NRR performance of the samples were augmented significantly as a function of applied potential up to -0.5 V *vs* RHE (Figure 3a), where the maximum NH_3 yield rate and FE were ~15.1 $\mu g \cdot cm^{-2} \cdot h^{-1}$ and 19% achieved on Au/CoO_x sample for 10 h, respectively. Above the optimum applied potential, the strong competitive adsorption of hydrogen species onto the sample surface accelerated the evolution of hydrogen, thereby suppressing the NRR. The other Au-based samples also displayed a similar potential dependence of the NH_3 yield rate and FE at different reaction times (Figures S22 and S23). Additionally, different to the control experiments that removed the Au NPs, replaced N_2 with Ar or cut off the applied potential, the NH_3 production on Au/CoO_x sample via electrochemical NRR increased progressively with increased reaction times (Figure S24), meaning the exclusion of contamination during production of NH_3. During an electrolysis period of up to 20 h, there is an approximately linear increase in NH_3 production using Au/CoO_x sample at prolonged reaction times, whereas a plateau in NH_3 production was observed after 20 h. This situation indicates that Au/CoO_x sample is stable for over ~20 h while functioning as an electrochemical NRR catalyst, as demonstrated in Figure S25. Furthermore, an FESEM image with line-scanning EDS data (Figure S26) only detected the Au NPs, with no EDS evidence of Co after electrolysis for 20 h. Actually, under acidic conditions and negative potentials, it is plausible that the CoO_x layer gradually dissolved into the electrolyte, noting that XPS detected that Co had disappeared from the surface of Au/CoO_x sample after 20 h NRR (Figure S27). Here, this underlines the critical roles of Au NPs in Au/CoO_x samples on the catalysis of the N_2-to-NH_3 fixation. Apart from ISE measurements, the indophenol blue method was also performed to determine the generation of NH_3 via NRR. The NH_3 yield rate as a function of applied potential on Au/CoO_x sample at 10 h of electrolysis is consistent with the aforementioned results (see Figures S28 and S29). In addition, ^{15}N isotopic labeling experiments were used to qualitatively and quantitatively verify the N source and NH_3 yield in NRR. To remove the impurities including few NH_3 gas and reducible labile nitrogen (like NO_x), isotope labeled $^{15}N_2$ gas was first flowed through a water-filled vessel with 0.1 M NaOH before bubbling into the H-type reaction cell. ^1H nuclear magnetic resonance (^1H NMR) spectra (Figure S30) showed that a doublet coupling with a spacing of ~73 Hz belongs to the signals of $^{15}NH_4^+$ as the feeding gas of $^{15}N_2$, while three symmetric signals of $^{14}NH_4^+$ are observed in the electrolyte with N_2. The intensity of $^{15}NH_4^+$ and $^{14}NH_4^+$ signals of the electrolyte on Au/CoO_x sample via NRR is stronger than that on Au sample, which is consistent with the results from ISE measurements. Meanwhile, there is no NMR signal of $^{15}NH_4^+$ and $^{14}NH_4^+$ in the electrolyte without electrodes passing through purged $^{15}N_2$ gas.

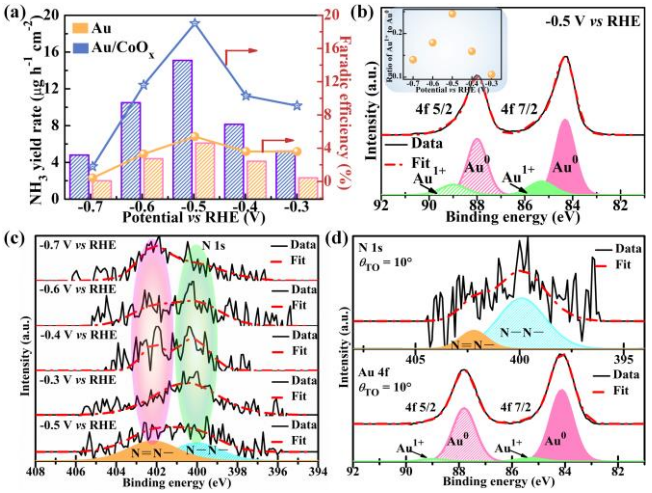

Figure 3. Catalytic performance of Au-based samples and evolution of the electronic structure after electrolysis. (a) NH_3 yield rate (column diagrams) and FE (point plots) on Au sample (orange) and Au/CoO_x sample (blue) at each given potential for 10 h. (b) Au 4f spectra of Au/CoO_x sample at θ_{TO} of 90° after 10 h of electrolysis at -0.5 V *vs* RHE. The inset shows the potential dependence of the ratio of Au^{1+} to Au^0 for Au/CoO_x sample after 10 h of electrolysis. (c) N 1s spectra of Au/CoO_x sample at θ_{TO} of 90° after 10 h electrolysis at different potentials. Taking -0.5 V *vs* RHE as an example, N 1s spectrum of Au/CoO_x sample can be deconvoluted into a superposition of two peaks shown as N=N- (orange) and N–N- (blue). (d) Au 4f (top) and N 1s (bottom) spectrum of Au/CoO_x sample at θ_{TO} of 10° after 10 h of electrolysis at -0.5 V *vs* RHE.

Having demonstrated the catalytic performance of Au NPs, we also explored the underlying mechanism associated with changes in Au oxidation state. Quasi in-situ XPS was employed to gather information about the electronic states, chemical bonding and oxidation states of Au-based sample surfaces exposed to electrolysis over 10 h. The Au 4f7/2 spectra of Au/CoO_x sample after electrolysis under given potentials showed two peaks at ~84.3 and ~85.3 eV corresponding to Au^0 and Au^{1+} (Figure 3b and Figure S31), which showed a positive chemical shift of about 0.4 and 0.2 eV compared to the original Au/CoO_x sample (its peaks at ~83.9 and ~85.1 eV), respectively. This down-field shift in the f-band center of Au reflects the formation of a hybridization band via a strong electronic effect[18] via Au NPs within an atomic range during NRR. Moreover, Au/CoO_x sample subjected to different applied potentials led to variations in the average oxidation state of Au, correlated with changes of in the efficacy of NRR. Among these conditions, Au/CoO_x sample held at -0.5 V *vs* RHE had the highest average oxidation state of Au (~0.25, which is approximately equal to the initial value), suggesting Au^{1+} may be stabilized at this applied potential over 10 h. By contrast, there are a few weak signals for N 1s on the surface of Au/CoO_x sample after electrolysis of 10 h (Figure 3c), which may be ascribed to a coupling of N_2 molecules on the surface of Au NPs, again correlated with shifts

in the binding energy of Au 4f core level. Using a Lorentzian-Gaussian distribution function, the N 1s spectra of Au/CoO_x sample subjected to different applied potentials were fitted into two peaks at ~400.2 and ~402.2 eV that are indicative of N–N– and N=N– active intermediates. A variation in the ratio of N=N– to N–N– with applied potential is correlated with changes in average oxidation state of Au as a consequence of NRR (Figure S32). This trend infers that the Au^{1+} active sites on Au NPs favour scission of the N≡N bond along with formation of N=N– intermediates via NRR, whilst Au^0 is the likely binding sites of N–N– intermediates, thereby implementing the subsequent hydrogenation reaction. Obviously, the binding strengths of N-based species on Au NPs is influenced by the applied potential. However, there was no XPS N 1s core level signal for the electrocatalyst surface after electrolysis in Ar atmosphere (Figure S33). In addition, the Au 4f and N 1s core level spectra at θ_{TO} of 10° on Au/CoO_x sample after electrolysis are shown in Figure 3d. It is clear that the intensities of Au^{1+} and N=N– XPS components decrease substantially for Au/CoO_x sample when θ_{TO} = 10°, again correlating with the relationship between Au^{1+} and N=N– and the distribution of Au^{1+} on Au NPs. Similarly, the XPS results for the other Au-based samples at -0.5 V *vs* RHE for 10 h (Figure S34) resembled the relationship between Au^{1+} and N=N– by comparison to the composition of Au/CoO_x sample.

DFT calculations have established that a CoO_x layer is a promising candidate to control the oxidation state of Au in light of charge exchange behaviour between cobalt oxide and gold (see Figure 4a). According to Bader charge analysis, there is a pronounced charge transfer from the Au_{10} cluster to the high valence Co, resulting in a margin of 0.26|e| positive charge on the bottom Au atoms (named Au^{1+}) in close proximity to CoO_x layer. In sharp contrast, the Au atoms at the top of Au_{10} cluster are retained in a charge state of metallic Au (named Au^0). These results demonstrate that Au atoms surrounded by a CoO_x layer are more predisposed to the generation of Au^{1+} sites than other Au atoms, suggesting that the architecture of Au NPs/CoO_x layer could offer a strategy for efficient modulation of oxidation states in Au catalysts.

To further elucidate the influence of Au^0 and Au^{1+} sites on the NRR performance of Au/CoO_x sample, we subsequently simulated the Gibbs free energy of the distal pathway for a catalyst comprising a Au_{10} cluster on a Co_3O_4 surface. Actually, based on the different hydrogenation sequences, an associative NRR mechanism is followed by distal and alternating pathways, respectively. In the distal pathway, the remote N atom is hydrogenated first and released as NH_3, whereas the two N atoms can be hydrogenated simultaneously to obtain two NH_3 molecules in the alternating pathway. However, in previous work[2c, 9], the distal pathway was shown to be energetically feasible for the Au-based catalytic systems. The free energy profiles and the corresponding atomic configurations of various states (*N_2, *NNH, *NNH_2, *N, *NH and *NH_2) on the Au^0 and Au^{1+} sites along the reaction route are displayed in Figure 4b. First of all, the absorption energy of N_2 molecule on Au^{1+} and Au^0 sites is 0.297 and 0.517 eV, respectively, implying a stronger interaction between N_2 molecule and Au^{1+} site. In general, the first hydrogenation step for the formation of *NNH is the rate-determining step (RDS). As a result, an uphill free energy change (ΔG) of RDS on Au^{1+} site is 1.82 eV, less than 2.40 eV achieved on Au^0 site, indicating that the *NNH can be easily connected to Au^{1+} site. In addition, the third step reacted from *NNH_2 to *N is more favourable on Au^{1+} site with a markedly lower ΔG of 1.57 eV, which is reduced by over a factor of 2 on the Au^0 site (ΔG of 3.52 eV). Decreasing the reaction energy required for the *NNH_2 + H → *N + NH_3 step can accelerate the conversion of N_2 to NH_3 and reduce the accumulation of *NNH_2. Furthermore, the ΔG value of the RDS on Au^{1+} sites is higher than that of the third reaction step, implying that more N=N– intermediates (*NNH) possibly stay at Au^{1+} sites in comparison to N–N– intermediates, which corroborates the results of the quasi in-situ XPS study. Taken together, these computational studies highlight that the introduction of Au oxidation state is an efficient approach for enhancement of the efficacy of N_2-to-NH_3 fixation.

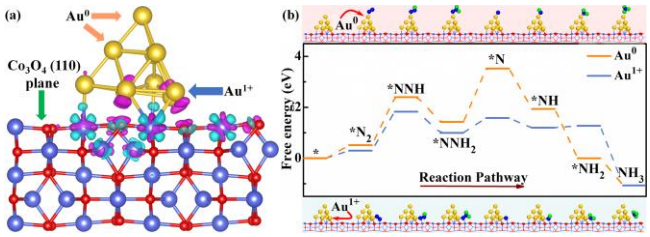

Figure 4. DFT computational studies of NRR on Au^0 and Au^{1+}. (a) Electron density difference of Au/CoO_x caused by anchoring of Au_{10} cluster. Cyan and pink isosurfaces represent electron accumulation and depletion, respectively. (b) Free energy profiles and optimized geometric structure schematic of NRR process (*N_2, *NNH, *NNH_2, *N, *NH and *NH_2) on Au^0 and Au^{1+} sites of Au/CoO_x sample following the distal mechanism. Au, Co, O, N and H atoms are labeled as gold, light blue, red, blue and green spheres in the optimized geometric structure schematic, respectively.

Conclusion

In conclusion. favourable conversion of N_2-to-NH_3 was achieved using Au NPs involving electron localization via a CoO_x supported layer. The behaviour of NRR as a function of Au oxidation state were evaluated, both experimentally and theoretically. At an average oxidation state of 40%, Au NPs showed a high faradic efficiency of 19% at -0.5 V *vs* RHE for NH_3 production. We believe that the introduction of metal with local electronic structure can offer a new direction for the fabrication of highly efficient catalysts and further extend our understanding on the mechanism of N_2-to-NH_3 fixation.

Experimental Section

The preparation, characterization, electrochemical measurement and calculation of the samples were performed as described in detail in the SI. Comprehensive experimental and computational details and methods can be found in the SI.

Acknowledgements

The authors are grateful to the National Natural Science Foundation of China (51402100, 21573066, 21825201 and 21805080), the China Postdoctoral Science Foundation, the Provincial Natural Science Foundation of Hunan (2016JJ1006 and 2016TP1009), the Shanghai Sailing Program (19YF1454300) and Australian Research Council (DP180100568 and DP180100731) for financial support of this research. Most of the computation was performaed on supercomputers of the National Supercomputer Centers in Changsha. We are also grateful for the support of the European Community's Seventh Framework Programme (FP7/2007-2013) under grant agreement № 312284 for research that was conducted on the Materials Science Beamline (MSB) at the Elettra Synchrotron. We also acknowledge Drs. Nataliya Tsud and Kevin C. Prince at the Elettra Synchrotron for assistance with the experiments. The authors acknowledge the CERIC-ERIC Consortium for access to experimental facilities and financial support. The CERIC-ERIC consortium and Czech Ministry of Education (LM2015057) are also acknowledged for financial support. RDM and JB thank the International Synchrotron Access Program of the Australian Synchrotron for travel funding to attend the experiment at the Elettra Synchrotron. In addition, we thank the facilities and scientific and technical assistance of the Curtin University Microscopy & Microanalysis Facility, WAX-ray Surface Analysis Facility, and XPS measurements from the John de Laeter Centre. Part of this research was undertaken with the EM instrumentation (ARC LE140100150) and XPS instrumentation (ARC LE120100026) at the John de Laeter Centre of Curtin University.

Keywords: N_2-to-NH_3 fixation • Au^{1+} oxidation state • N_2 adsorption • high activity and selectivity

[1] a) R. F. Service, *Science* **2014**, *345*, 610-610; b) R. F. Service, *Science* **2018**, *361*, 120-123.

[2] a) D. Bao, Q. Zhang, F. L. Meng, H. X. Zhong, M. M. Shi, Y. Zhang, J. M. Yan, Q. Jiang, X. B. Zhang, *Advanced materials* **2017**, *29*, 1604799; b) M. Ali, F. L. Zhou, K. Chen, C. Kotzur, C. L. Xiao, L. Bourgeois, X. Y. Zhang, D. R. MacFarlane, *Nature Communications* **2016**, *7*, 11335; c) Y. Yao, S. Q. Zhu, H. J. Wang, H. Li, M. H. Shao, *J Am Chem Soc* **2018**, *140*, 1496-1501.

[3] a) M. Nazemi, S. R. Panikkanvalappil, M. A. El-Sayed, *Nano Energy* **2018**, *49*, 316-323; b) M. Nazemi, M. A. El-Sayed, *Journal of Physical Chemistry Letters* **2018**, *9*, 5160-5166.

[4] S. J. Li, D. Bao, M. M. Shi, B. R. Wulan, J. M. Yan, Q. Jiang, *Advanced materials* **2017**, *29*, 1700001.

[5] a) J. Deng, J. A. Iñiguez, C. Liu, *Joule* **2018**, *2*, 846-856; b) L. Wang, M. Xia, H. Wang, K. Huang, C. Qian, C. T. Maravelias, G. A. Ozin, *Joule* **2018**, *2*, 1055-1074.

[6] a) P. De Luna, R. Quintero-Bermudez, C. T. Dinh, M. B. Ross, O. S. Bushuyev, P. Todorović, T. Regier, S. O. Kelley, P. Yang, E. H. Sargent, *Nature Catalysis* **2018**, *1*, 103-110; b) Y. Y. Liang, H. L. Wang, P. Diao, W. Chang, G. S. Hong, Y. G. Li, M. Gong, L. M. Xie, J. G. Zhou, J. Wang, T. Z. Regier, F. Wei, H. J. Dai, *J Am Chem Soc* **2012**, *134*, 15849-15857; c) H. Xiao, W. A. Goddard, T. Cheng, Y. Y. Liu, *P Natl Acad Sci USA* **2017**, *114*, 6685-6688.

[7] a) Y. S. Zhou, F. L. Che, M. Liu, C. Q. Zou, Z. Q. Liang, P. De Luna, H. F. Yuan, J. Li, Z. Q. Wang, H. P. Xie, H. M. Li, P. N. Chen, E. Bladt, R. Quintero-Bermudez, T. K. Sham, S. Bals, J. Hofkens, D. Sinton, G. Chen, E. H. Sargent, *Nature Chemistry* **2018**, *10*, 974-980; b) F. S. Roberts, K. P. Kuhl, A. Nilsson, *Angew Chem Int Edit* **2015**, *54*, 5179-5182.

[8] A. J. Martín, T. Shinagawa, J. Pérez-Ramírez, *Chem* **2019**, *5*, 263-283.

[9] J. Zheng, Y. Lyu, M. Qiao, R. Wang, Y. Zhou, H. Li, C. Chen, Y. Li, H. Zhou, S. P. Jiang, S. Wang, *Chem* **2019**, *5*, 1-17.

[10] J. Zheng, Y. Lyu, R. Wang, C. Xie, H. Zhou, S. P. Jiang, S. Wang, *Nature Communications* **2018**, *9*, 3572.

[11] J. Fester, A. Makoveev, D. Grumelli, R. Gutzler, Z. Z. Sun, J. Rodriguez-Fernandez, K. Kern, J. V. Lauritsen, *Angew Chem Int Edit* **2018**, *57*, 11893-11897.

[12] a) D. D. Sarma, P. K. Santra, S. Mukherjee, A. Nag, *Chemistry of Materials* **2013**, *25*, 1222-1232; b) V. Papaefthimiou, T. Dintzer, V. Dupuis, A. Tamion, F. Tournus, D. Teschner, M. Havecker, A. Knop-Gericke, R. Schlogl, S. Zafeiratos, *Journal of Physical Chemistry Letters* **2011**, *2*, 900-904.

[13] R. Parameswaran, J. L. Carvalho-de-Souza, Y. W. Jiang, M. J. Burke, J. F. Zimmerman, K. Koehler, A. W. Phillips, J. Yi, E. J. Adams, F. Bezanilla, B. Z. Tian, *Nature Nanotechnology* **2018**, *13*, 260-266.

[14] C. Miron, M. Patanen, *Advanced materials* **2014**, *26*, 7911-7916.

[15] J. Y. Zheng, S. H. Bao, Y. Guo, P. Jin, *ACS Appl Mater Interfaces* **2014**, *6*, 1351-1355.

[16] P. N. Duchesne, Z. Y. Li, C. P. Deming, V. Fung, X. J. Zhao, J. Yuan, T. Regier, A. Aldalbahi, Z. Almarhoon, S. W. Chen, D. E. Jiang, N. F. Zheng, P. Zhang, *Nature Materials* **2018**, *17*, 1033-1039.

[17] J. Zheng, Y. Lyu, C. Xie, R. Wang, L. Tao, H. Wu, H. Zhou, S. Jiang, S. Wang, *Advanced materials* **2018**, *30*, 1801773.

[18] C. Z. Li, Q. Yuan, B. Ni, T. He, S. M. Zhang, Y. Long, L. Gu, X. Wang, *Nature Communications* **2018**, *9*, 3702.

Entry for the Table of Contents (Please choose one layout)

Layout 1:

RESEARCH ARTICLE

Tuning the local electronic structure of Au nanoparticles with positive valence sites can boost conversion of N_2 to NH_3 via control of N_2 adsorption and the concomitant energy barrier of NRR. The introduction of metal with local electronic structure can offer a new direction on the fabrication of highly efficient catalysts for NRR.

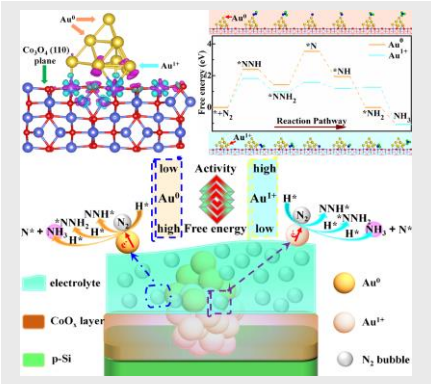

Jianyun Zheng,[†][a],[b] *Yanhong Lyu,*[†][a] *Man Qiao,*[†][c] *Jean P. Veder,*[d] *Roland D. Marco,*[b],[e],[f] *John Bradley,*[e] *Ruilun Wang,*[a] *Yafei Li,*[*][c] *Aibin Huang,*[*][g],[h] *San Ping Jiang,*[*][b] *Shuangyin Wang*[*][a]

Page No. – Page No.

Electron localization of gold in control of nitrogen-to-ammonia fixation